RAA 2019 Vol. **19** No. **12**, 186(18pp) doi: 10.1088/1674–4527/19/12/186

http://www.raa-journal.org *http://iopscience.iop.org/raa*

***R**esearch in*
***A**stronomy and*
***A**strophysics*

Forecasts of cosmological constraints from HI intensity mapping with FAST, BINGO and SKA-I

Elimboto Yohana[1,2,3,4], Yi-Chao Li[3,4] and Yin-Zhe Ma[3,4]

[1] Astrophysics and Cosmology Research Unit, School of Mathematics, Statistics & Computer Science, University of KwaZulu-Natal, Westville Campus, Private Bag X54001, Durban, 4000, South Africa; *ey@tssfl.com*
[2] Dar Es Salaam University College of Education, A Constituent College of the University of Dar Es Salaam, P.O. Box 2329 Dar Es Salaam, Tanzania
[3] Astrophysics and Cosmology Research Unit, School of Chemistry and Physics, University of KwaZulu-Natal, Westville Campus, Private Bag X54001, Durban, 4000, South Africa
[4] NAOC-UKZN Computational Astrophysics Centre (NUCAC), University of KwaZulu-Natal, Durban, 4000, South Africa

Received 2019 February 20; accepted 2019 July 17

Abstract We forecast the cosmological constraints of the neutral hydrogen (HI) intensity mapping (IM) technique with radio telescopes by assuming 1-year of observational time. The current and future radio telescopes that we consider here are Five-hundred-meter Aperture Spherical radio Telescope (FAST), Baryon acoustic oscillations In Neutral Gas Observations (BINGO), and Square Kilometre Array phase I (SKA-I) single-dish experiments. We also forecast the combined constraints of the three radio telescopes with *Planck*. We find that the 1σ errors of (w_0, w_a) for BINGO, FAST and SKA-I with respect to the fiducial values are respectively, $(0.9293, 3.5792)$, $(0.4083, 1.5878)$ and $(0.3158, 0.4622)$. This is equivalent to $(56.04\%, 55.64\%)$ and $(66.02\%, 87.09\%)$ improvements in constraining (w_0, w_a) for FAST and SKA-I respectively relative to BINGO. Simulations further show that SKA-I will put more stringent constraints than both FAST and BINGO when each of the experiments is combined with *Planck* measurements. The 1σ errors for (w_0, w_a), BINGO + *Planck*, FAST + *Planck* and SKA-I + *Planck* covariance matrices are respectively $(0.0832, 0.3520)$, $(0.0791, 0.3313)$ and $(0.0678, 0.2679)$ implying there is an improvement in (w_0, w_a) constraints of $(4.93\%, 5.88\%)$ for FAST + *Planck* relative to BINGO + *Planck* and an improvement of $(18.51\%, 23.89\%)$ in constraining (w_0, w_a) for SKA-I + *Planck* relative to BINGO + *Planck*. We also compared the performance of *Planck* data plus each single-dish experiment relative to *Planck* alone, and find that the reduction in (w_0, w_a) 1σ errors for each experiment plus *Planck*, respectively, imply the (w_0, w_a) constraints improvement of $(22.96\%, 8.45\%)$, $(26.76\%, 13.84\%)$ and $(37.22\%, 30.33\%)$ for BINGO + *Planck*, FAST + *Planck* and SKA-I + *Planck* relative to *Planck* alone. For the nine cosmological parameters in consideration, we find that there is a trade-off between SKA-I and FAST in constraining cosmological parameters, with each experiment being more superior in constraining a particular set of parameters.

Key words: surveys — galaxies: statistics — cosmology: observations — large-scale structure of Universe — galaxies: kinematics and dynamics

1 INTRODUCTION

Cosmology has improved our understanding of the Universe over the last few decades. Up to this time, study of the Universe has mostly given us a basic picture of how the Universe evolved and formed its large-scale structure (LSS). Many experiments dedicated to studying the Universe throughout its entire history at various epochs have been conducted while others are ongoing or planned to take off in the near future. Some of the most notable surveys targeting the LSS of the Universe include a number of galaxy redshift surveys such as the Two-degree-Field Galaxy Redshift Survey (2dFGRS, Colless et al. 2001), the WiggleZ Dark Energy Survey (Blake et al. 2008, 2011; Kazin et al. 2014), the Six-degree-Field Galaxy Survey (6dFGS, Jones et al. 2009; Beutler et al. 2011) and the

Baryon Oscillation Spectroscopic Survey (BOSS, Ross et al. 2012), which is part of the third stage of the Sloan Digital Sky Survey (SDSS, York et al. 2000; Anderson et al. 2012; Alam et al. 2017). Recently, the Dark Energy Survey (DES), (Dark Energy Survey Collaboration et al. 2016) reported their cosmological constraints with the 1-year data (Troxel et al. 2018; Camacho et al. 2019). Future optical surveys that aim to utilize larger and more sensitive telescopes at a variety of high redshifts, such as Dark Energy Spectroscopic Instrument (DESI) (Levi et al. 2013; DESI Collaboration et al. 2016), Large Synoptic Survey Telescope (LSST) (Ivezić et al. 2019; LSST Science Collaboration et al. 2009; The LSST Dark Energy Science Collaboration et al. 2018), *Euclid* (Laureijs et al. 2011) and *WFIRST* (Green et al. 2012), have been proposed and some of the constructions are under way. To date, galaxy-redshift surveys have made significant progress in surveying the LSSs of the Universe. To do precision cosmology, one would need to detect sufficiently large samples of HI-emitting galaxies. However, this is a huge task, since at higher redshifts the galaxies look essentially very faint (Bull et al. 2015b; Kovetz et al. 2017; Pritchard & Loeb 2012).

In radio astronomy, observation of the 21 cm spectrum line emitted by neutral hydrogen (HI) in deep space provides a rich tool for understanding cosmic evolution. After the cosmic reionization, the hydrogen outside galaxies was ionized. However, a massive amount of HI shielded from ionizing ultraviolet photons resided within the dense gas clouds embedded in galaxies as these gas clouds cooled and collapsed to form stars. As a result, the quantity and distribution of HI are related to the evolution of galaxies and cosmic surveys in the radio band, whose origin and evolution are highly related to the structure formation history and nature of cosmic expansion (Pritchard & Loeb 2012; Kovetz et al. 2017).

At lower redshift $z \lesssim 0.1$, HI can be detected with the 21 cm emission and absorption lines from its hyperfine splitting. At redshift greater than 2.2, HI can also be detected via optical observation of the Lyα absorption line against bright background sources (Zwaan et al. 2004; Haynes 2008). At intermediate redshift, the 21 cm emission line of each individual galaxy is too faint to be detected. However, instead of cataloging individual galaxies, the intensity mapping (IM) method measures the total HI flux from many galaxies, and can be applied to LSS studies (Chang et al. 2008; Loeb & Wyithe 2008). With the HI IM method, Chang et al. (2010) first reported the measurements of cross-correlation function between the HI map, observed with the Green Bank Telescope (GBT) and the DEEP2 optical redshift survey (Davis et al. 2001). With the extended GBT HI survey and WiggleZ Dark Energy Survey, the cross-power spectrum between HI and optical galaxy survey was also detected (Masui et al. 2013). Recently, another HI survey with the Parkes telescope reported the measurements of cross-power spectrum with the 2dF optical galaxy survey (Anderson et al. 2018). So far, the auto-power spectrum of the HI IM survey is still not detected (Switzer et al. 2013) because of contamination from the foreground residuals.

There are a number of current and future experiments targeting HI IM. These experiments are increasingly comprised of wide-field and sensitive radio telescopes or interferometers, such as Baryon acoustic oscillations In Neutral Gas Observations (BINGO, Dickinson 2014), Canadian Hydrogen Intensity Mapping Experiment (CHIME, Bandura et al. 2014), Tianlai (Chen 2012) and Hydrogen Intensity and Real-time Analysis eXperiment (HIRAX, Newburgh et al. 2016). Besides the specially designed telescopes or interferometers, several larger single-dish telescopes and interferometers, such as the Five-hundred-meter Aperture Spherical radio Telescope (FAST, Nan et al. 2011), Square Kilometre Array (SKA, Bull et al. 2015a; Santos et al. 2015; Braun et al. 2015) or MeerKAT (Santos et al. 2017), are also planned for HI IM survey.

This paper aims to use HI IM to forecast how future HI experiments, such as BINGO, FAST and SKA Phase I (SKA-I), will constrain various cosmological parameters.

FAST is the world's largest single-dish telescope and features high resolving power. BINGO is a medium sized single-dish telescope with a special design (Battye et al. 2016). SKA-I is a telescope array which, in single-dish autocorrelated mode, is suitable for probing large volumes over very large cosmological scales. These experiments are the next-generation LSS surveys, which can be employed to develop and verify improved techniques for HI IM surveys. Our aim is to simultaneously consider three experiments whose nature and designs categorically represent many future HI IM probes. We will present quantitative and qualitative comparison between their future prospects, while addressing the range of expected performances, limitations and challenges that may accompany these experiments.

We develop a forecast framework that is motivated and guided by physical experimental design and set-ups, which can be correctly transformed into mathematics and computer simulations. We believe that this clear scientifically motivated forecast study will substantially provide testable predictions and determine paths and feasibility for future HI IM experiments.

The outline of the paper is as follows. In Section 2, we briefly describe the three future experiments, namely, BINGO, FAST and SKA-I. In Section 3, we discuss and summarize the mathematical derivation of the tomographic angular power spectrum and introduce the thermal noise power spectrum as residuals of various contaminants af-

ter applying foreground removal techniques. This spectrum of noise is related to various observable experimental parameters. We further show the calculation of noise power spectrum in Section 3.2 and tomographic power spectrum to compute the Fisher matrix in Section 3.3. Noise power spectrum together with tomographic angular power spectrum are prime tools for computing the Fisher matrix via maximum likelihood estimation (MLE) (Dodelson 2003; Shaw et al. 2015). We present forecasts of cosmological constraints in Section 4 based on various cosmological parameters of our choice and analyze the results. In this section, we also define the cosmological parameters implemented and present various FAST, BINGO and SKA-I experimental parameter specifications. We summarize our forecasts in Section 5. Finally, we conclude our paper in Section 6.

Unless otherwise stated, we adopt a spatially-flat Λ cold dark matter (ΛCDM) cosmology model with fiducial parameters listed in Table 1 (Planck Collaboration et al. 2014, 2016).

2 INTENSITY MAPPING PROJECTS

BINGO, FAST and SKA-I experiments are potentially suitable for surveying HI intensity maps of the Universe and are open avenues for doing a wide range of sciences. In this section, we briefly describe each of these three future experiments for studying the IM of HI.

2.1 BINGO

The BINGO project is proposed to be built in Brazil and aims to map HI emission at redshift range $0.13 - 0.48$ ($960\,\mathrm{MHz} \sim 1260\,\mathrm{MHz}$). BINGO will map an approximately 15° strip of the sky to measure the HI power spectrum and detect, for the first time, baryon acoustic oscillations (BAOs) at radio frequencies. BINGO's expected design is a dual-mirror compact antenna test range telescope with a $40\,\mathrm{m}$ primary mirror and an offset focus, which is proposed to have a receiver array containing between 50 - 60 feed horns, with a $90\,\mathrm{m}$ focal length. For more details about the construction of BINGO and its prospective capabilities, please refer to Battye et al. (2013); Bigot-Sazy et al. (2015); Battye et al. (2016).

2.2 FAST

FAST is a ground-based radio telescope built within a karst depression in Guizhou province of southwest China. The L-band receiver is designed for 19 beams and the multi-beam receiver will increase the survey speed (Nan et al. 2011). FAST is believed to be the most sensitive single dish telescope currently in existence, covering a wide frequency range from $70\,\mathrm{MHz} - 3\,\mathrm{GHz}$ and a potentially large area of up to $25\,000\,\mathrm{deg}^2$. Here, we consider a survey area of $10\,000\,\mathrm{deg}^2$, approximately equivalent to the one used by Alam et al. (2015). The chosen survey area reasonably suffices for our current study, and is regarded as moderate considering other experimental parameters and design factors. In addition, this choice is also potentially suitable for any future FAST-SDSS cross-correlation studies. For the HI IM survey with FAST, we consider a frequency range of $950\,\mathrm{MHz} \sim 1350\,\mathrm{MHz}$. FAST has a diameter of 500 meters but the illuminated aperture is 300 meters. For full details on FAST engineering and its capabilities, please refer to Nan et al. (2011); Smoot & Debono (2017).

2.3 SKA-I

The SKA project, currently under development, is basically an interferometry array. The project plans two stages of development, comprising SKA Phase I and SKA Phase II (Bull et al. 2015a; Santos et al. 2015; Braun et al. 2015). The first stage (SKA Phase I) radio astronomy facility is split and shared between South Africa (SKAI-MID) – hosted in the Karoo Desert, and an aperture array in Australia, SKA-LOW Phase I (SKAI-LOW). SKAI-MID plans to build 133 $15\,\mathrm{m}$ diameter dishes and will incorporate 64 dishes from the MeerKAT array (Santos et al. 2017; Fonseca et al. 2017), each with $13.5\,\mathrm{m}$ diameter, that have already been constructed in the Karoo Desert. Note that SKA-I telescope specifications implemented for our study have been subject to changes as the project has gone through various levels of revision (Bull 2016), see recent updates in Square Kilometre Array Cosmology Science Working Group et al. (2018). Due to the weak resolution requirement for HI IM, we ignore the cross correlation between dishes, which means the SKAI-MID array is working as 133 single dishes, with an extension of 64 $13.5\,\mathrm{m}$ MeerKAT array dishes. We therefore consider tentative experimentation with SKAI-MID Band 1 (excluding the MeerKAT array), hereafter referred to as SKA-I, at frequencies $350\,\mathrm{MHz} \sim 1050\,\mathrm{MHz}$ for the full 133 antennae for a total survey area of $10\,000\,\mathrm{deg}^2$. However, we make the same choice of survey area as for FAST for similar reasons as explained in Subsection 2.2. For full details about BINGO, FAST and SKA-I experimental design, see Table 2.

3 METHOD

3.1 Tomographic Angular Power Spectrum

In our forecast, we consider the tomographic angular power spectrum of HI for the i-th and j-th redshift bins given by

$$C_\ell^{ij} = 4\pi T_b^{ij} \int \mathrm{d}\ln k \Delta^2(k) \Delta^W_{T_\mathrm{b},\ell}(k) \Delta^{W'}_{T_\mathrm{b},\ell}(k), \quad (1)$$

Table 1 Cosmological Parameters in Our Study as the Best-fitting Parameters in Planck Collaboration et al. (2016)

Parameter	Fiducial value	Description
$\Omega_{\rm b}h^2$	0.0226	Fractional baryon density today
$\Omega_{\rm c}h^2$	0.112	Fractional cold dark matter density today
w_0	-1.00	Dark energy EoS, from the relationship $w(a) = w_0 + (1-a)w_a$
w_a	0.00	Dark energy EoS, from the relationship $w(a) = w_0 + (1-a)w_a$
$\ln(10^{10}A_{\rm s})$	3.089	Log power of the primordial curvature perturbations, ($k_0 = 0.05\,{\rm Mpc}^{-1}$)
H_0	70.00	The Hubble constant (current expansion rate in km s^{-1} Mpc^{-1})
$N_{\rm eff}$	3.046	Effective number of neutrino-like relativistic degrees of freedom
$n_{\rm s}$	0.96	Scalar spectrum power-law index ($k_0 = 0.05\,{\rm Mpc}^{-1}$)
$\Sigma m_\nu/94.07$ eV	0.00064	The sum of neutrino masses in eV

Table 2 Experiment Parameters for FAST, BINGO and SKA-I

	FAST	SKA-I	BINGO
$\nu_{\rm min}$[MHz]	950	350	960
$\nu_{\rm max}$[MHz]	1350	1050	1260
$\Delta\nu$[MHz]	10	10	10
$n_\nu(n_z)$	40	70	30
$D_{\rm dish}$[m]	300	15	25
$N_{\rm ant} \times N_{\rm feed}$	1×19	133×1	1×60
$t_{\rm TOT}$[yr]	1	1	1
$T_{\rm rec}$[K]	25	Eq. (8)	50
$S_{\rm survey}$[deg^2]	10 000	10 000	3000

$D_{\rm dish}$ is the illuminated aperture (Li & Ma 2017).

where $\Delta^2(k)$ is the dimensionless power spectrum of primordial curvature perturbation. Here, $T_{\rm b}^{ij} = T_{\rm b}(z_i)T_{\rm b}(z_j)$ is the multiplication of HI mean brightness temperature (Chang et al. 2008) of the i-th and j-th redshift bins, with

$$T_{\rm b}(z) = 0.39\,{\rm mK}\left(\frac{\Omega_{\rm HI}}{10^{-3}}\right)\left(\frac{1+z}{2.5}\right)^{0.5} \times \left(\frac{\Omega_{\rm m}+(1+z)^{-3}\Omega_\Lambda}{0.29}\right)^{-0.5} \quad (2)$$

where $\Omega_{\rm HI}$ is the fraction of HI density assumed to be 0.62×10^{-3} (Switzer et al. 2013) and $\Delta^W_{T_{\rm b},\ell}(k) \equiv \Delta^W_{T_{\rm b},\ell}(\mathbf{h})/\mathcal{R}(\mathbf{k})$ (Hall et al. 2013). The transfer function is

$$\Delta^W_{T_{\rm b},\ell}(\mathbf{k}) = \int_0^\infty {\rm d}z W(z)\Delta_{T_{\rm b},\ell}(\mathbf{k},z), \quad (3)$$

which is an integration of the temperature fluctuation over the bandwidth $W(z)$. The temperature fluctuation for each ℓ (projected mode) for each wavenumber $\mathbf{k}$ and redshift bin z is

$$\begin{aligned}\Delta_{T_{\rm b},\ell}(\mathbf{k},z) = {}& \delta_n j_\ell(k\chi) + \frac{kv}{\mathcal{H}}j''_\ell(k\chi) \\ & + \left(\frac{1}{\mathcal{H}}\dot\Phi + \Psi\right)j_\ell(k\chi) \\ & - \left(\frac{1}{\mathcal{H}}\frac{{\rm d}\ln(a^3\bar n_{\rm HI})}{{\rm d}\eta} - \frac{\dot{\mathcal{H}}}{\mathcal{H}^2} - 2\right) \\ & \times \big[\Psi j_\ell(k\chi) + v j'_\ell(k\chi) \\ & + \int_0^\chi \left(\dot\Psi + \dot\Phi\right) j_\ell(k\chi'){\rm d}\chi'\big],\end{aligned} \quad (4)$$

where j_ℓ is the spherical Bessel function, δ_n is the HI density contrast and the second term $kvj''_\ell(k\chi)/\mathcal{H}$ is the redshift space distortion term (Hall et al. 2013).

Here, we work in the tomographic power spectrum in ℓ-space of multiple redshift (frequency) slices. We notice that there are several previous works which implemented the forecasts in three-dimensional (3-D) k-space (Bull et al. 2015a,b). There are some advantages that the tomographic two-dimensional power spectrum in $\ell-$space has compared to the 3-D power spectrum in k-space. The 3-D power spectrum in k-space has the following disadvantages:

- It assumes plane-parallel conditions, so it cannot encompass wide angle correlations;
- It cannot include lensing effect, either;
- In the analysis of 3-D power spectrum, the redshift bins are typically wide, which neglects the evolution of background within bins; and
- It requires a fiducial model which must be assumed to relate redshift to distance.

In addition, the tomographic angular power spectrum can easily be applied to perform cross-correlations between 21 cm images and other LSS tracers at the same redshift. Due to these reasons, our approach thus has some advantages over a 3-D power spectrum, and we find it worthy investigating as we have done so in this work. Full details regarding the advantages of using the tomographic angular power spectrum can be referenced in Shaw & Lewis

(2008); Di Dio et al. (2014); Tansella et al. (2018); Camera et al. (2018).

3.2 Noise

Noise for the single-dish IM experiment is given by

$$N_\ell^{ij} = \delta^{ij} N_\ell^{\rm HI} = \frac{\delta^{ij} T_{\rm sys}^2 S_{\rm survey}}{(N_{\rm ant} N_{\rm feed} t_{\rm TOT} \Delta\nu)}, \quad (5)$$

where $N_{\rm ant}$ is the number of antennae, $N_{\rm feed}$ is the total number of feed horns and $t_{\rm TOT}$ is the total observational time.

BINGO and FAST system temperatures are expressed as

$$T_{\rm sys} = T_{\rm rec} + T_{\rm sky}, \quad (6)$$

whereas the SKA-I system temperature is modeled by adding ground spill-over (Square Kilometre Array Cosmology Science Working Group et al. 2018)

$$T_{\rm sys} = T_{\rm rec} + T_{\rm spl} + T_{\rm sky}. \quad (7)$$

Here, $T_{\rm spl} \approx 3$ K is the spill-over contribution.

Furthermore, $T_{\rm rec}$ is the receiver temperature particular to each telescope model. The BINGO and FAST receiver temperatures are presented in Table 2, where for SKA-I

$$T_{\rm rec} = 15\ {\rm K} + 30\ {\rm K}(\nu({\rm GHz}) - 0.75)^2. \quad (8)$$

Basically, all three telescopes see the same sky, so we model their sky temperature contribution as

$$T_{\rm sky} = T_{\rm gal} + T_{\rm CMB}, \quad (9)$$

with

$$T_{\rm gal} \approx 25\ {\rm K}(408\ {\rm MHz}/\nu)^{2.75} \quad (10)$$

being the contribution from our Milky Way Galaxy for a given frequency ν and $T_{\rm CMB} \approx 2.73$ K is the cosmic microwave background (CMB) temperature. One can refer to Square Kilometre Array Cosmology Science Working Group et al. (2018) for more information regarding system temperature, and Table 2 for the detailed list of exact values of each experimental parameter considered in our forecast.

Generally speaking, 21 cm intensity maps highly suffer from contaminations due to foregrounds, such as Galactic synchrotron emission, extragalactic point sources and atmospheric noises. Thus, applications of foreground cleaning techniques are inevitably important in order to mitigate these contaminations. However, there is always some level of contamination residuals after applying such techniques. Therefore, the cross-correlation of noises between different frequency bins may not completely be negligible. So, the elements of the noise matrix N_ℓ have been treated under some simplified assumptions (Li & Ma 2017).

3.3 Fisher Matrix

We perform the Fisher matrix analysis to explore the potential of future HI IM experiments for constraining the cosmological parameters. Assuming that the MLE can be approximated well by a multivariate Gaussian function, the Fisher matrix $\mathcal{F}$ is then a good approximation of the inverse of the parameter covariance matrix. The Fisher matrix is expressed as,

$$\mathcal{F}_{\alpha\beta} = f_{\rm sky} \sum_{\ell_{\rm min}}^{\ell_{\rm max}} \left(\frac{2\ell+1}{2}\right) {\rm tr}\left[C_{\ell,\alpha} \Sigma_\ell C_{\ell,\beta} \Sigma_\ell\right], \quad (11)$$

in which the total noise inverse matrix is given by

$$\Sigma_\ell = (C_\ell + N_\ell)^{-1}. \quad (12)$$

Here, N_ℓ, the noise power spectrum, is an $n_\nu \times n_\nu$ matrix. We assume that noises between the i-th and j-th frequency channels ($i \neq j$) are uncorrelated, and thus N_ℓ is a diagonal matrix. The tomographic angular power spectrum, C_ℓ, is an $n_\nu \times n_\nu$ matrix, and each element of C_ℓ is the HI cross angular power spectrum of the i-th and j-th redshift bins. Furthermore, we multiply C_ℓ with the window function for the i, j-th frequency channels,

$$W_{\ell,ij} = {\rm e}^{-\ell^2\left(\sigma_i^2 + \sigma_j^2\right)/2}, \quad (13)$$

which is simply the multiplication of the Fourier space Gaussian beam function at the i-th and j-th frequency channels. In this case,

$$\sigma_i = \theta_{\rm FWHM}/(\sqrt{8\ln(2)}) \simeq 0.4245\theta_{\rm FWHM}, \quad (14)$$

where $\theta_{\rm FWHM} = 1.22\lambda/D_{\rm dish}$ is the full-width at half maximum (FWHM) of the beam. The window function (13) implies that, at large values of ℓ, corresponding to small angular scales, it falls off rapidly as depicted by the HI angular power spectra in Figure 1.

For all cosmological constraints, we ignore the monopole and dipole moments, and consider a multipole moment range from $\ell = 2$ to $\ell = 600$ for forecast with BINGO and SKA-I, and $\ell = 2$ to $\ell = 1000$ for FAST. This range of ℓ is chosen for each telescope to ensure that, within each range of ℓ, the signal-to-noise ratio (SNR) is significant, which contributes to the constraints of cosmological parameters. For very high ℓ, the beam function makes the signal be below the noise power spectrum, so adding high-ℓ of the power spectrum does not improve the constraints.

Here, we vary nine parameters which are shown in Table 1. Therefore, our Fisher matrix (Eq. (11)) is a 9×9 matrix. To see how we can tighten up constraints with *Planck* satellite data, we utilized the best-fit ΛCDM CMB power spectra from the baseline *Planck* chains, which include TT + TE + EE + lensing, taken from the Planck

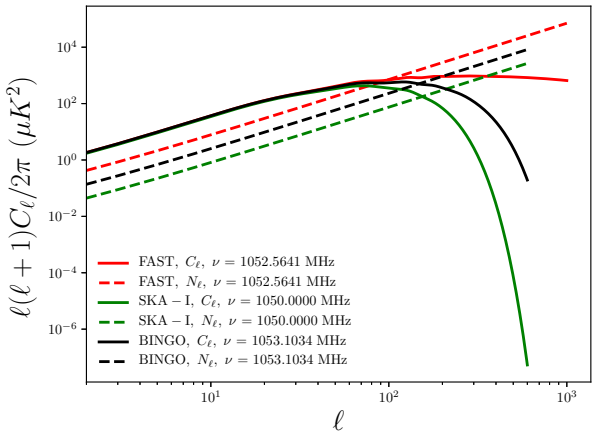

Fig. 1 The noise power spectra N_ℓ (*dashed lines*) and beam convolved angular power spectra, C_ℓ (*solid lines*) for FAST (*red*), BINGO (*black*) and SKA-I (*green*) at approximately overlapped frequencies. As expected, we see that the angular power spectra have almost the same profile at large scales but deviate with increase in number of multipoles, ℓ. Beyond $\ell = 150$, angular power spectra for BINGO and SKA-I more rapidly become insignificant than noise compared to FAST angular power spectrum.

Legacy Archive website – Cosmology section [1] to compute the *Planck* covariance. We then make an entry-wise addition of the *Planck* Fisher matrix (the inverse of the *Planck* covariance (Planck Collaboration et al. 2016)) for each parameter, to the corresponding parameter entries in the resulting Fisher matrix calculated by applying the formulae (11) for each particular HI IM experiment. The model cosmological parameters whose values were varied by making entry-wise addition of the *Planck* Fisher matrix correspondingly to BINGO, FAST and SKA-I Fisher matrices are $\Omega_{\rm b}h^2$, $\Omega_{\rm c}h^2$, w_0, w_a, $\ln(10^{10}A_{\rm s})$, H_0 and $n_{\rm s}$. The rest of the HI experiment parameters, namely, $N_{\rm eff}$ and $\Sigma m_\nu/94.07$ eV, were omitted so that we could only consider parameters that conform with the *Planck* chains dataset, Planck Collaboration et al. (2016) (believed to set the strongest constraints on cosmological parameters), that we used to compute the *Planck* Fisher matrix under consideration.

4 RESULTS AND DISCUSSION

In this section, we present two sets of forecast results, the first one detailing a comparison on various cosmological constraints between FAST, BINGO and SKA-I, and the second one showing relative constraining capabilities by combining each of the three experiments with *Planck*. The *Planck* covariance matrix includes TT + TE + EE + lensing, but throughout this paper, we will use a shorthand *Planck* to mean *Planck* + TT + TE + EE + lensing. Table 3 lists the 1σ errors for the marginalized parameter constraints for each of these experiments. In our simulations, for all the three experiments, we fix the frequency bandwidth to be 10 MHz, unless stated otherwise. More specifically, the frequency (or equivalently redshift) division is done with uniform spacing of channels, each with width 10 MHz or 1 MHz, depending on the tests performed, This means that for standard tests carried out with a channel width of 10 MHz, we included 30 redshift/frequency bins for BINGO, 40 redshift bins for FAST and 70 redshift bins for SKA-I, while for tests carried out with a 1 MHz channel width, we used 300, 400 and 700 redshift bins, respectively, for BINGO, FAST and SKA-I. We have defined significantly narrower channel width compared to most of the previous works, for the motivation described in the later sections. Roughly, the central value of each channel width was used in calculations, which is the sum of the lower and upper margins divided by 2. The central value of the bin is a good approximation for sufficiently narrower bins in that we can neglect evolution of cosmological functions/backgrounds within each redshift bin, because most of the relevant functions coupled in calculations of the angular power spectra vary slowly with redshift; instead, the evolving cosmological functions are fixed to their values at the central redshift of the bin, the choice of which is however motivated by Bull et al. (2015b). Full telescope specifications we implemented for simulations are presented in Table 2, and the descriptions of the cosmological parameters utilized in the forecast are given in Table 1. We use `Camb_sources` (Challinor & Lewis 2011) to compute the raw tomographic angular power spectra Equation (1) and another code that we developed to simulate forecasts of cosmological parameter constraints via Fisher matrix (Subsection 3.3). We will then compare the forecasted constraints between these different experiments.

4.1 Dark Energy Constraints

We present two separate analyses, the first one is to show how FAST, BINGO and SKA-I can comparatively constrain the dark energy equation of state (EoS) in the form of $w(a) = w_0 + w_a(1-a)$ ("Chevallier-Polarski-Linder parametrization" (Chevallier & Polarski 2001; Linder 2003)) and the second one is to indicate how each of these experiments, FAST, BINGO and SKA-I plus *Planck* data, can constrain the dark energy EoS. Figure 2 demonstrates that FAST will constrain the dark energy EoS better than BINGO, and possibly than many other currently known single-dish HI IM approach counterparts. However, SKA-I puts more stringent constraints on the dark energy EoS than both BINGO and FAST. The 1σ errors from (w_0, w_a) covariance matrices for BINGO, FAST and SKA-

[1] `https://pla.esac.esa.int/#cosmology`

I are, respectively, $(0.9293, 3.5792)$, $(0.4083, 1.5878)$ and $(0.3158, 0.4622)$.

To compare the relevant improvement in 1σ errors from BINGO to FAST and SKA-I, we consider the largest error of the three experiments for a particular parameter and find out the fractions of the errors that have been reduced with respect to it. For w_0, the error is reduced by $(0.9293 - 0.4083)/0.9293 = 56.06\%$ and $(0.9293 - 0.3158)/0.9293 = 66.02\%$ for FAST and SKA-I with respect to BINGO, respectively. For w_a, it is $(3.5792 - 1.5878)/3.5792 = 55.64\%$ and $(3.5792 - 0.4622)/3.5792 = 87.09\%$ for FAST and SKA-I with respect to BINGO, respectively. Therefore, we can see quite significant improvement of FAST and SKA-I for future constraints on dark energy EoS. Although the parameters w_0 and w_a have some degeneracy, the joint constraints with *Planck* can significantly improve the constraints.

The fact that FAST will do better than BINGO to constrain the dark energy EoS remains unchanged if each of the experiments is individually combined with *Planck* data, as shown in Figure 3. This observation is valid and is supported by Bigot-Sazy et al. (2016), although in their paper they applied a different set of experimental parameters. As previously observed from simulations in Figure 2, again, Figure 3 demonstrates that SKA-I will put more stringent constraints than both FAST and BINGO when each of the experiment's Fisher matrix is added to the *Planck* Fisher matrix. The 1σ errors for (w_0, w_a), BINGO + *Planck*, FAST + *Planck* and SKA-I + *Planck* covariance matrices are, respectively, $(0.0832, 0.3520)$, $(0.0791, 0.3313)$ and $(0.0678, 0.2679)$, implying (w_0, w_a) constraints improve by $(4.93\%, 5.88\%)$ in error reduction for FAST + *Planck* relative to BINGO + *Planck* and there is an improvement of $(18.51\%, 23.89\%)$ in error reduction when constraining (w_0, w_a) for SKA-I + *Planck* relative to BINGO + *Planck*, see Table 3. It is clear that all three experiments improve dark energy constraints tremendously when the *Planck* Fisher matrix is added to each of the respective experiment's Fisher matrix.

To benchmark the performance of each single-dish experiment combined with *Planck* relative to *Planck* alone, we find that the $(w_0, w_a)1\sigma$ errors for *Planck*, BINGO + *Planck*, FAST + *Planck* and SKA-I + *Planck* are respectively, (0.1080, 0.3845), (0.0832, 0.3520), (0.0791, 0.3313) and (0.0678, 0.2679). The reduction in $(w_0, w_a)1\sigma$ errors for each experiment plus *Planck*, respectively, implies an improvement in the (w_0, w_a) constraints of (22.96%, 8.45%, (26.76%, 13.84%) and (37.22%, 30.33%) for BINGO + *Planck*, FAST + *Planck* and SKA-I + *Planck* relative to *Planck* alone. Table 3, Figure 11 and Figure 13 summarize how the *Planck*-each-single-dish experiment joint constraints improve relative to the *Planck* data constraints alone for all the cosmological parameters considered.

To investigate the optimal survey volume, we consider FAST and SKA-I, and explore the range of survey areas from $2000\,\mathrm{deg}^2$ to $25\,000\,\mathrm{deg}^2$. Considering (w_0, w_a) constraints, we find the optimal survey area is around $16\,000\,\mathrm{deg}^2$ for FAST with $T_{\rm sys}$ corresponding to $T_{\rm rec} = 25\,\mathrm{K}$ and $9000\,\mathrm{deg}^2$ for a $T_{\rm sys}$ corresponding to $T_{\rm rec} = 35\,\mathrm{K}$. Results show that SKA-I can survey up to a maximum area of $25\,000\,\mathrm{deg}^2$. This reality can be illustrated by the figure of merit (FoM) depicted in Figure 4. FoM is defined as (Huterer & Turner 2001; Albrecht & Bernstein 2007)

$$\mathrm{FoM} \propto [\sigma(w_0)\sigma(w_a)]^{-1} \propto 1/\sqrt{\det C(w_0, w_a)}. \quad (15)$$

We vary the survey area and see which $\Omega_{\rm sur}$ can maximize the FoM. As previously stated, we choose the survey area of $10\,000\,\mathrm{deg}^2$ that was covered by the SDSS (Alam et al. 2015). The choice has a benefit of being fairly moderate and is potentially suitable for comparative and cross-correlation studies involving SDSS-like experiments, FAST and SKA-I. In addition, it is practical to choose this survey area for FAST and SKA-I comparisons because the marginal increase of FAST FoM is quite small if $\Omega_{\rm sur} > 10\,000$, so we will use $\Omega_{\rm sur} = 10\,000$ in our forecast. BINGO (Bigot-Sazy et al. 2015) can survey an approximate area of $2500\,\mathrm{deg}^2 - 3000\,\mathrm{deg}^2$ as reported by Li & Ma (2017); Bigot-Sazy et al. (2016), but for this particular study, we use a survey area of $3000\,\mathrm{deg}^2$ as was suggested by Bigot-Sazy et al. (2016).

Generally speaking, higher system temperature will result in higher noise spectra, which makes the constraints worse. This is indicated well by the FoM (Fig. 4), as signified by the two FAST system temperatures, $T_{\rm sys}$ of 25 K and 35 K. Low values of $1/\sqrt{\det C(w_0, w_a)}$ at high system temperature mean that experimental performance decreases with an increase in system temperature. For this reason, it is likely that BINGO is mostly affected because of its high overall system temperature.

There are several reasons why SKA-I performs better than both BINGO and FAST to constrain the dark energy EoS. One of the reasons is the SKA-I's wide range of frequency coverage. We split the SKA-I frequency range into lower frequency band $350\,\mathrm{MHz} \sim 700\,\mathrm{MHz}$ and higher frequency band $700\,\mathrm{MHz} \sim 1050\,\mathrm{MHz}$, and compare them with the full SKA-I frequency range ($350\,\mathrm{MHz} \sim 1050\,\mathrm{MHz}$). As plotted in Figure 5, the full SKA-I range of frequencies proportionately puts more stringent constraints on w_0 and w_a than lower and upper frequency bands, and the FoM improves significantly, as illustrated in Figure 6. The reason is that the full frequency range of SKA-I includes the measurement of HI power spectrum at a larger range of redshift evolution, and also includes the

Table 3 1σ errors for FAST, BINGO, SKA-I and *Planck* covariance matrices, and those obtained from covariance matrices resulting from a combination of each of the FAST, BINGO and SKA-I experiment's Fisher matrix with *Planck* Fisher matrix.

	FAST	BINGO	SKA-I	*Planck*	FAST + *Planck*	BINGO + *Planck*	SKA-I + *Planck*
$\Omega_{\rm b}h^2$	0.0090	0.0168	0.0072	0.0002	0.0001	0.0001	0.0001
$\Omega_{\rm c}h^2$	0.0061	0.0133	0.0115	0.0014	0.0011	0.0012	0.0008
w_0	0.4083	0.9293	0.3158	0.1080	0.0791	0.0832	0.0678
w_a	1.5878	3.5792	0.4622	0.3845	0.3313	0.3520	0.2679
$\ln(10^{10}A_{\rm s})$	0.1681	0.3217	0.2209	0.0271	0.0240	0.0259	0.0146
H_0	3.6902	6.5433	4.0082	1.0341	0.5288	0.6171	0.5282
$N_{\rm eff}$	1.7016	3.3814	1.2486	––	––	––	––
$n_{\rm s}$	0.0201	0.0727	0.0550	0.0046	0.0043	0.0045	0.0039
$\Omega_\nu h^2$	0.0044	0.0048	0.0017	––	––	––	––

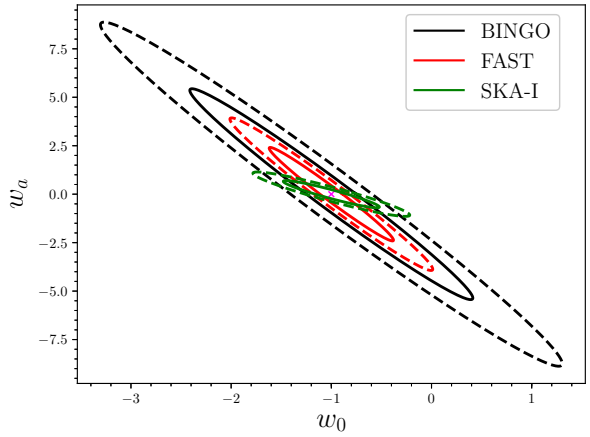

Fig. 2 w_0 versus w_a, 1σ (*solid lines*) and 2σ (*dashed lines*) cosmological constraints for FAST (*red*), BINGO (*black*) and SKA-I (*green*).

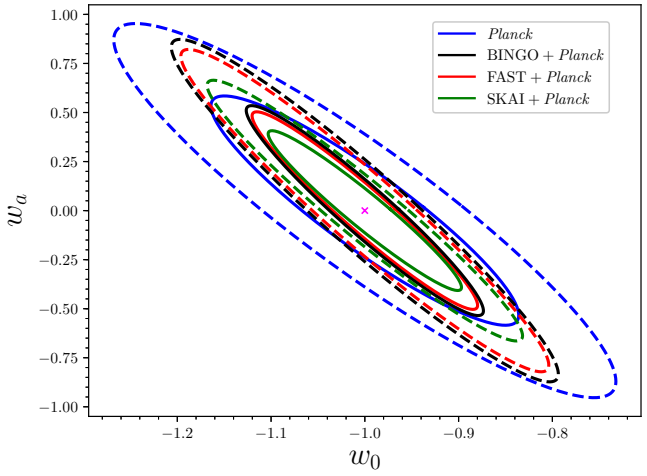

Fig. 3 w_0 versus w_a, 1σ (*solid lines*) and 2σ (*dashed lines*) cosmological constraints for *Planck* (*blue*), FAST + *Planck* (red), BINGO + *Planck* (*black*) and SKA-I + *Planck* (*green*).

information on cross-correlated signals in higher and lower frequency bands. Therefore, it provides tighter constraints than higher and lower redshift bands.

Moreover, as we have previously accounted for BINGO, system temperature seems to be an important nuisance, which if not controlled, will hamper constraints. The less stronger constraints for the lower half of the frequency band of SKA-I compared to the upper band in Figure 5 (see also Fig. 6) are suggestively due to high system temperatures at the corresponding frequencies. The system temperature is somewhat a function of frequency, especially parts of $T_{\rm sys}$ (Eq. (7)) that vary with it, i.e. Equations (8) and (9). As a result, we see that system temperature, $T_{\rm sys}$, is more dominant at low frequencies than at high frequencies, see Figure 7. This effect can also be noted for the FAST FoM at different system temperatures, see Figure 4.

The current SKA-I experimental design is to have 133 15-meter dishes and 64 13.5-meter MeerKAT dishes. We illustrate the forecast with SKA-I by considering the previous number of dishes, which is 190, and then compare the constraint forecasts with the updated number of dishes, which is 133. The reason for considering the former num-

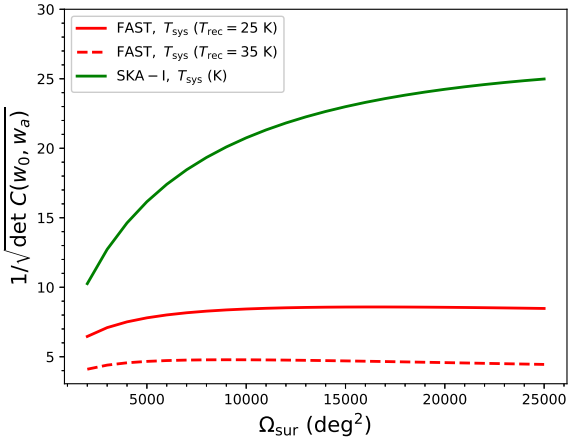

Fig. 4 FoM: inverse square root of the determinant of w_0, w_a covariance matrix, $1/\sqrt{\det C(w_0, w_a)}$ versus survey area, $\Omega_{\rm sur}$ (deg^2) for FAST (*red*) at system temperatures, $T_{\rm rec}$, of 25 K (*solid line*) and 35 K (*dashed line*), and for SKA-I (*green*) at system temperature, $T_{\rm sys}$ (K), given by Eq. (7).

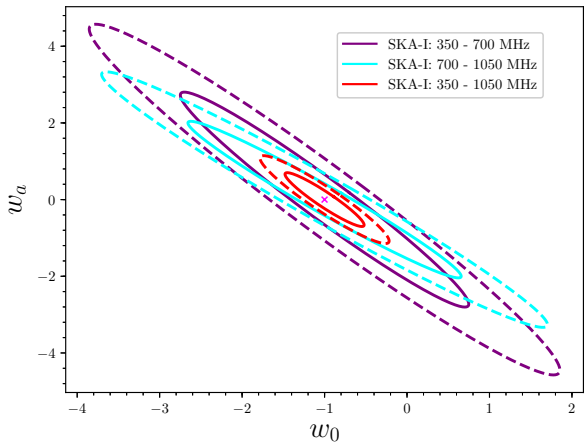

Fig. 5 w_0 versus w_a, 1σ (*solid lines*) and 2σ (*dashed lines*) cosmological constraints for SKA-I split into lower frequency band (*purple*), high frequency band (*cyan*) and full range (*red*) of SKA-I frequencies.

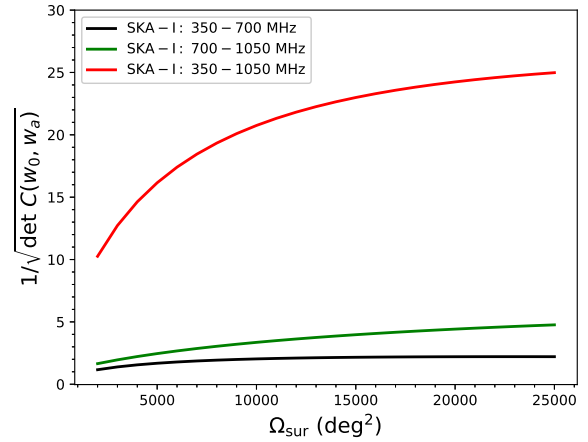

Fig. 6 FoM: inverse square root of the determinant of w_0, w_a covariance matrix, $1/\sqrt{\det C(w_0, w_a)}$ versus survey area, $\Omega_{\rm sur}$ (deg^2) for various SKA-I frequency bands: lower frequency band, $350-700$ MHz (*black*), upper frequency band, $700-1050$ MHz (*green*) and the full SKA-I frequency range, $350-1050$ MHz (*red*).

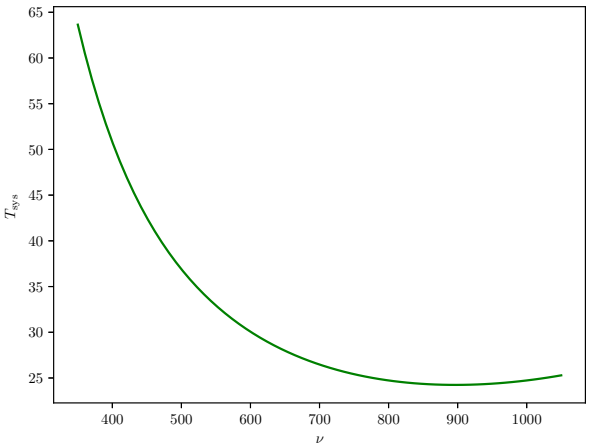

Fig. 7 SKA-I variation of system temperature, $T_{\rm sys}$ against frequency, ν.

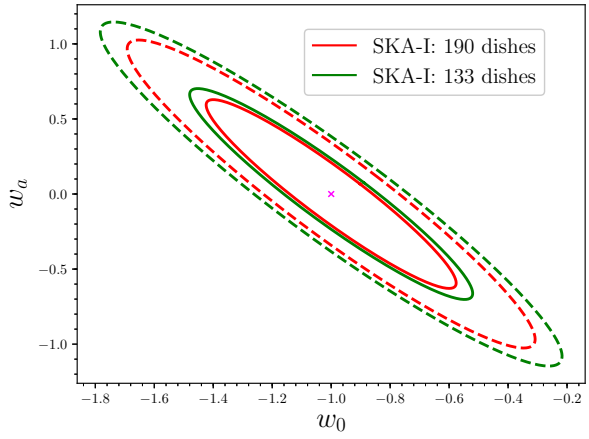

Fig. 8 1σ (*solid lines*) and 2σ (*dashed lines*) comparisons of SKA-I (SKAI-MID Band I) constraints on the dark energy EoS by considering the early proposition of 190 dishes (*red*) and the updated (*green*) 133 dishes.

ber of dishes is to illustrate how the change in the number of dishes affects performance, and also to form a reference point for comparison with previous literature that considered old SKA-I (SKAI-MID) experimental specifications.

We see from Figure 8 that constraints do not strongly respond to the number of dishes. The most intrinsic property of a large number of dishes is mapping LSS at very large angular distances/scales by integrating HI emission efficiently over large volumes slices of the sky. One would expect that a large number of dishes would significantly improve cosmological constraints, but if we compare constraints by assuming SKAI-MID 190 and on the other hand 133 single dishes, both in the autocorrelation mode, we notice that there is not much significant difference.

The exact procedure of how to incorporate images from different frequency bands is unknown (Square Kilometre Array Cosmology Science Working Group et al. 2018), but in this forecast we assume that the SKA-I project incorporates 190 15-meter single-dishes in an autocorrelated mode for HI IM.

4.2 Constraints on other cosmological parameters

We present the results of our forecast for the nine cosmological parameters in Table 1 for the single dish experiments: FAST (Nan et al. 2011; Bigot-Sazy et al. 2016), BINGO (Bigot-Sazy et al. 2015; Battye et al. 2012) and the SKA-I (Bull et al. 2015a; Santos et al. 2015). Figure 9 displays the constraints on various cosmological parameters.

For the case of dark energy EoS, we have seen that SKA-I will give the strongest constraints followed by FAST and then BINGO.

Considering all nine parameters, SKA-I and FAST are competitive in their abilities in constraining cosmological parameters. As illustrated in Figure 9, FAST provides stronger constraints on $n_{\rm s}$ because its larger dish can supply more constraints on small-scales of HI power spectra. Interestingly, the marginalized constraints on $n_{\rm s}$ for BINGO and SKA-I do not show much significant difference. FAST will also impose stronger constraints on $\Omega_{\rm c}h^2$, $\ln(10^{10}A_{\rm s})$ and H_0 than both BINGO and SKA-I, but slightly better constraint on H_0 than SKA-I. In comparison, SKA-I will strongly constrain $\Omega_\nu h^2$ in addition to w_a, while slightly better constraining $\Omega_{\rm b}h^2$ and w_0 parameters than FAST. Another observation is that SKA-I imposes slightly stronger bounds on both $N_{\rm eff}$ joint and marginalized constraints than FAST. The corresponding $\Omega_\nu h^2$, $N_{\rm eff}$ and $\Omega_{\rm b}h^2$ 1σ errors for SKA-I, respectively, reduce by 61.36%, 26.62% and 20% relative to FAST. Likewise, the corresponding 1σ errors for the parameters where FAST performs better than SKA-I, $n_{\rm s}$, $\Omega_{\rm c}h^2$, H_0 and $\ln(10^{10}A_{\rm s})$ respectively, are reduced by 63.45%, 46.96%, 7.93% and 23.9% relative to the corresponding SKA-I 1σ errors. These reductions in the errors proportionately imply improvements in constraints as reflected by simulations. In Figure 10, we depict the relative constraint improvement in percentage for all parameters and for the three simulated experiments.

The prospective better performance of FAST in constraining particular parameters, as we have seen, is due to its high angular resolving power. FAST has the largest dish diameter of the three telescopes which means its angular resolution is higher than that of SKA-I and BINGO by a factor of 21 and 7.5 respectively, making it very capable of mapping signals at small angular scales. So, it is likely that FAST's performance will be significant at small scales. On the other hand, Figure 1 indicates FAST is noise-dominated for $\ell > 100$, because its SNR is less than unity, while SKA-I does not attain SNR<1 until $\ell > 150$. This suggests that SKA-I may better constrain cosmological parameters at some ranges of small angular scales due to its higher SNR compared to FAST on those scales. Although SNR for SKA-I is greater than unity until $\ell > 150$, from this point onwards, SKA-I SNR decreases exponentially, while SNR for FAST decreases gently across the same range of scales. This elucidates another important clue that both FAST and SKA-I can perform relatively well in constraining cosmological parameters sensitive to small angular scales. As we have previously pointed out, the trade-off on whether FAST or SKA-I can perform better at small scales may not be determined by a single factor but may be influenced by a number of factors, such as the choice of parameterization.

For the case of dark energy constraints, stringent constraints for SKA-I are due to its wider frequency coverage than FAST and BINGO. BINGO is probably disadvantaged due to its high system/receiver noise temperature.

Figure 11 visualizes cosmological constraints for each of these experiments combined with *Planck* by using a Fisher matrix forecast. At this instance, constraints for all the three experiments improve significantly. As we have seen, SKA-I + *Planck* continues to provide better constraints than FAST + *Planck* and BINGO + *Planck* on dark energy EoS parameters w_0 and w_a. In contrast to the previous case involving FAST, BINGO and SKA-I experiments, SKA-I + *Planck* constraints on $\ln(10^{10}A_{\rm s})$ and $\Omega_{\rm c}h^2$ relative to FAST + *Planck* and BINGO + *Planck* experiments are now very significant. Similarly, neither FAST + *Planck* nor SKA-I + *Planck* shows significant improvement in constraining $\Omega_{\rm b}h^2$ compared to BINGO + *Planck*. Therefore, SKA-I + *Planck* imposes strong constraints on $\Omega_{\rm c}h^2$ and $\ln(10^{10}A_{\rm s})$, in addition to w_0, w_a, as we have ascertained previously, relative to FAST + *Planck* and BINGO + *Planck*.

More specifically, SKA-I + *Planck* manifests some significant improvement in constraining $\Omega_{\rm c}h^2$ and $\ln(10^{10}A_{\rm s})$ than FAST + *Planck* and BINGO + *Planck* by respectively, 27.27%, 39.17% and 33.33%, 43.63%. However, SKA-I + *Planck* is, respectively, slightly better in constraining $n_{\rm s}$ than FAST + *Planck* and BINGO + *Planck* by 9.3% and 13.33%.

In a like manner, FAST + *Planck* exhibits some significant improvement in constraining $\Omega_{\rm c}h^2$, w_0, w_a, $\ln(10^{10}A_{\rm s})$, H_0 and $n_{\rm s}$ than BINGO + *Planck* by 8.33%, 4.93%, 5.88%, 7.34%, 14.31% and 4.44%, respectively.

Though there is significant performance improvement in constraining most of the cosmological parameters for FAST + *Planck* compared to FAST alone, for SKA-I + *Planck* compared to SKA-I alone and for BINGO + *Planck* compared to BINGO alone, there is no improvement for FAST + *Planck* in constraining H_0 relative to SKA-I + *Planck*, see Figures 11 and 12.

As we have seen from Figures 11 and 12, SKA-I + *Planck*, followed by FAST + *Planck*, is more competitive in constraining cosmological parameters than BINGO + *Planck*. In any case, *Planck* results have a very significant impact on constraining cosmological parameters when combined with each of the three experiments (Fig. 13).

In addition, we have tested using the dark energy EoS and find that, for BINGO, FAST and SKA-I HI IM experiments, the choice of frequency channel width $\Delta\nu = 1\,$MHz can significantly improve constraints for all the three HI experiments than larger channel width (Fig. 14). This is because a smaller bandwidth can preserve the

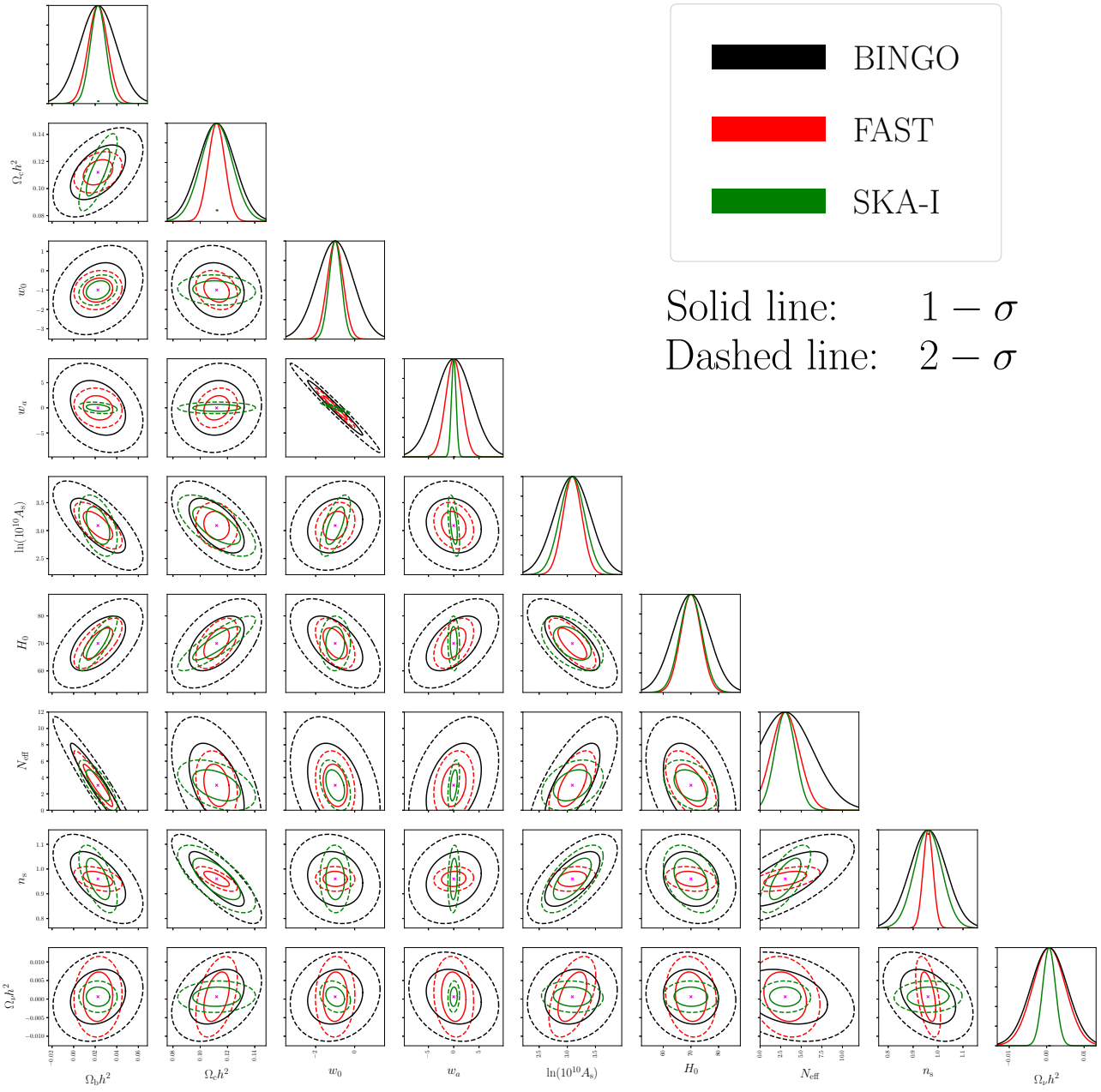

Fig. 9 Forecasts of cosmological constraints from future observations with FAST, BINGO and SKA-I.

redshift-space-distortion effect in the radial direction, which makes it less "Limber canceled" than wider bandwidth (Hall et al. 2013). This is also illustrated in figure 6 of Xu et al. (2018).

To strike a balance between limitation of foreground techniques to extract HI signal at high angular scales and constraint prospects, as a case study, we simulate new dark energy EoS constraints by ignoring multipole moments at large angular scales, up to $\ell = 9$. The comparisons between Figures 2 and 3 simulated by considering full multipole range of our interest, and Figures 15 and 16 where we apply multipole moments cut-off, by considering minimum $\ell = 10$, yield a conflicting scenario between foreground effects if we ignore small ℓ's and optimistic constraint forecast if we include them. Neglecting several values of ℓ corresponding to large angular scales weakens constraints, and the 1σ errors for marginalized (w_0, w_a) constraints change, respectively, for BINGO, FAST and SKA-I from (0.9293, 3.5792), (0.4083, 1.5878), (0.3158, 0.4622) to (1.0250, 3.9449), (0.4355, 1.6864), (0.4059, 0.5735); and from (0.0832, 0.3520), (0.0791, 0.3313), (0.0678, 0.2679) to (0.0835, 0.3532), (0.0795, 0.3336), (0.0702, 0.2776) for BINGO + *Planck*, FAST + *Planck* and SKA-I + *Planck*, as summarized in Table 4.

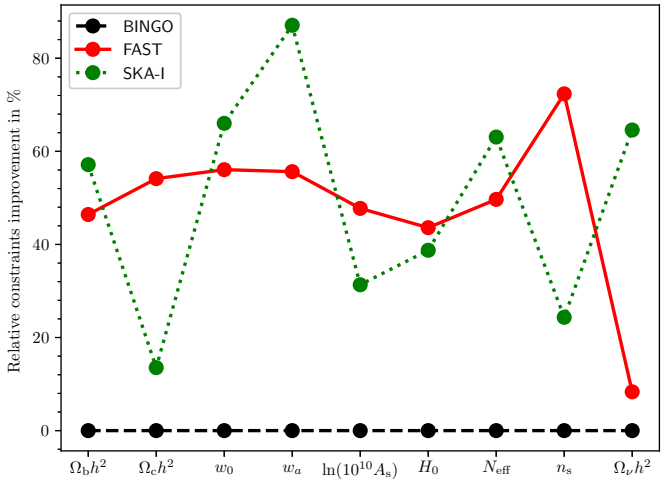

Fig. 10 The relative percentage improvement for FAST and SKA-I with respect to BINGO in constraining each of the nine cosmological parameters.

Table 4 1σ errors for FAST, BINGO and SKA-I covariance matrices, and those obtained from covariance matrices resulting from a combination of each of the FAST, BINGO and SKA-I experiment's Fisher matrix with *Planck* Fisher matrix, for minimum multipole moments, $\ell = 2$ and $\ell = 10$. Errors signify that constraints resulting from discarding small values of ℓ, i.e., $2 \leq \ell < 10$, equivalent to large angular scales, are weaker than those including small ℓ's.

	FAST	BINGO	SKA-I	FAST + *Planck*	BINGO + *Planck*	SKA-I + *Planck*
$\ell \geq 2$						
w_0	0.4083	0.9293	0.3158	0.0791	0.0832	0.0678
w_a	1.5878	3.5792	0.4622	0.3313	0.3520	0.2679
$\ell \geq 10$						
w_0	0.4355	1.0250	0.4059	0.0795	0.0835	0.0702
w_a	1.6864	3.9449	0.5735	0.3336	0.3532	0.2776

This is a clear illustration of how large angular scales that are more dominated by the foreground contaminations may affect the cosmological constraint forecast analyses. However, we will assume that the ongoing progress in circumventing the foreground challenge and bias at large scales and other systematics at both large and small scales will be successful, and hence allow us to consider the maximum possible range of ℓ's, as we have done in this study.

The subject of foreground in general, its domination and challenges faced by its removal on certain angular scales have been discussed in Wolz et al. (2014, 2015); Alonso et al. (2015) and the references therein; whereby Planck Collaboration et al. (2018) present a comparative study on the performance of a number of algorithms for diffuse component separation, just to name a few.

The current study is primarily focused on forecast of cosmological parameter constraints with HI IM experiments. To this point, we postpone the in-depth discussion of the challenge presented by foregrounds to the next issue of this series. Such issues include addressing systematic limitations such as contaminations of single-dish observations by what is so called $1/f$ noise, a single instrumental systematic, due to frequency correlation, and the correlated gain fluctuations across the receiver bandpass (Harper et al. 2018).

5 COMPARISON WITH PREVIOUS FORECASTS OF HI IM

This forecast aims to optimize the potential of future 21 cm IM experiments, by providing an in-depth comparative objective study focusing on FAST, BINGO and SKA-I in autocorrelation mode, operating as a collection of independent single-dish (rather than usual interferometry) telescopes. We use much cleaner and explicit maximum likelihood and Fisher matrix tools to forecast the behavior of these three telescopes by considering a wide range of sensitive experimental analyses aspects, laying formalism that can be employed to forecast varying sets of cosmological parameter constraints with a diverse range of 21 cm IM experiments. We notice that there are several previous studies that have made cosmological forecasts for HI IM experiments, but our paper has the following distinctive features:

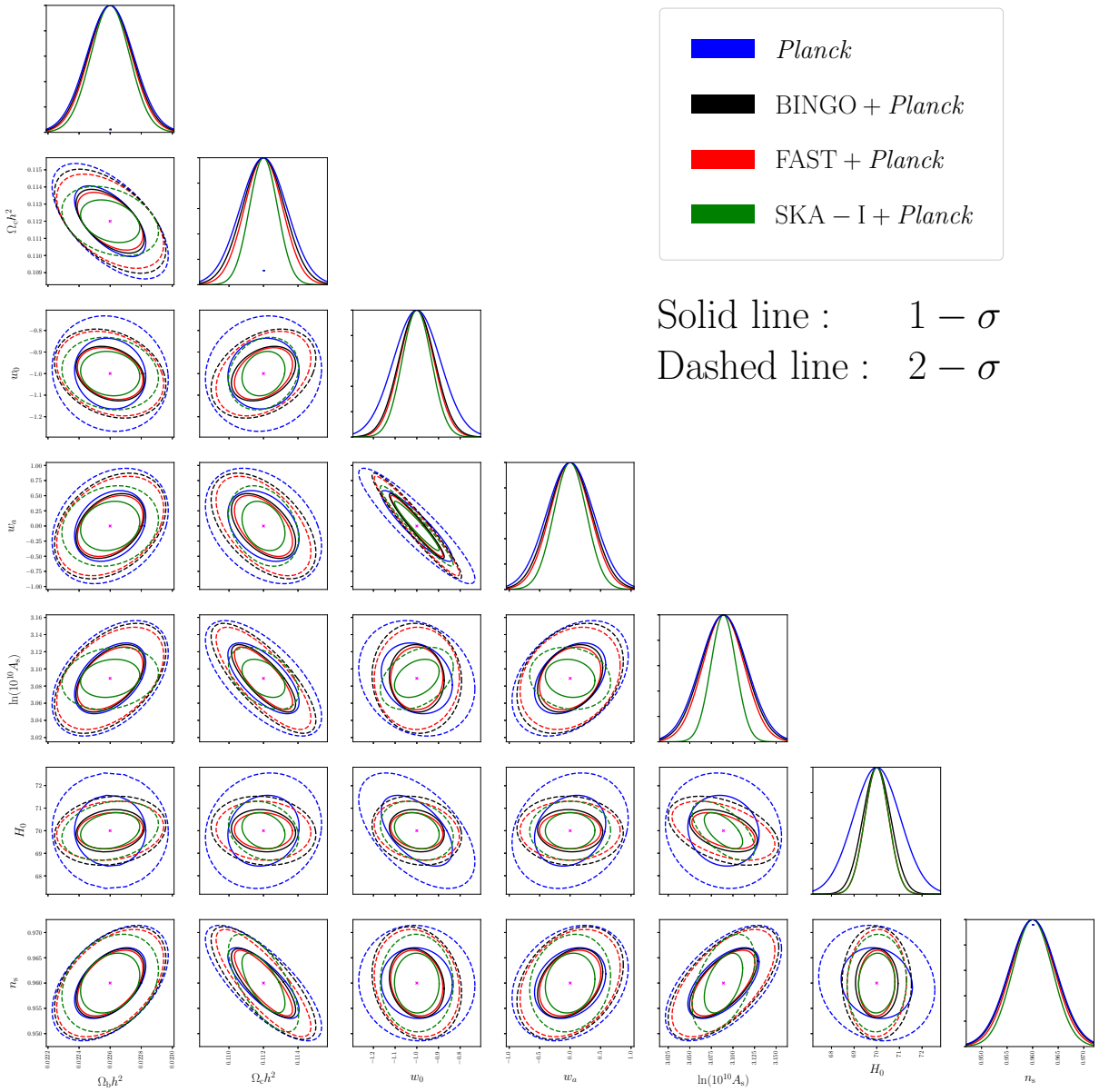

Fig. 11 Forecasts of joint cosmological constraints with each of the FAST, BINGO and SKA-I experiments plus *Planck* data, compared with *Planck* data constraints alone.

– Extending the work by Bull et al. (2015b) to consider different cosmological parameter sets. Bull et al. (2015b) considered a set from the standard ΛCDM model: the Hubble parameter, $H_0 = 100h\,\mathrm{km\,s^{-1}\,Mpc^{-1}}$, the cosmological constant, Ω_Λ, the baryon density, $\Omega_\mathrm{b}h^2$, the linear amplitude of density fluctuations, σ_8, the index of the power spectrum of primordial density fluctuations, n_s, and the optical depth to last scattering, τ. They extended the ΛCDM model with parameters w_0, w_a, Ω_K and the growth index, γ. Here the cosmological constant, Ω_Λ, and the curvature parameter, Ω_K, are related to the total matter density (cold dark matter + baryons) by $\Omega_\mathrm{M} = 1 - \Omega_\mathrm{K} - \Omega_\Lambda$. In their forecast, they used varying subsets of the considered parameter set to measure constraints. Their forecast approach included fixing fiducial values of some parameters, marginalizing over the *Planck* priors in the Fisher matrix or over other parameters, and not directly constraining some parameters by assuming their strong correlation with other parameters, such as in the case of *Planck* priors, where *Planck* measurements were combined with a particular experiment. We extended a subset of parameters considered in the aforementioned paper to form a new set, Table 1, and carried out Fisher matrix forecast, derived and treated under a somewhat different approach. However, we expanded both cosmological parameters and the HI IM set of experi-

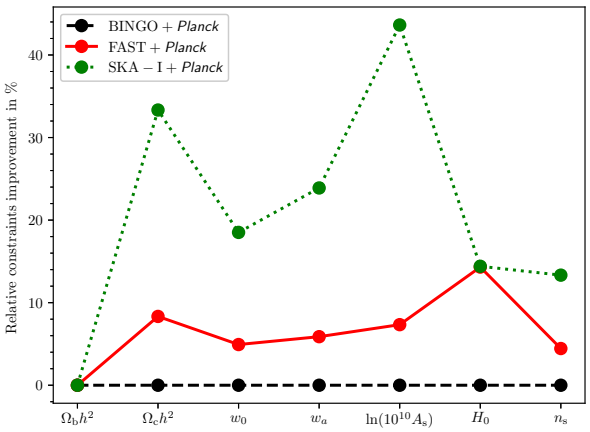

Fig. 12 The relative percentage improvement for FAST + *Planck* and SKA-I + *Planck* with respect to BINGO + *Planck* in constraining each of the seven cosmological parameters we have considered.

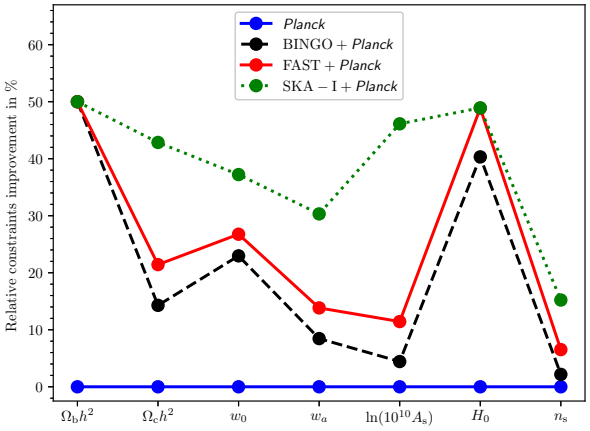

Fig. 13 The relative percentage improvement for BINGO + *Planck*, FAST + *Planck* and SKA-I + *Planck* with respect to *Planck* alone in constraining each of the seven cosmological parameters we have considered.

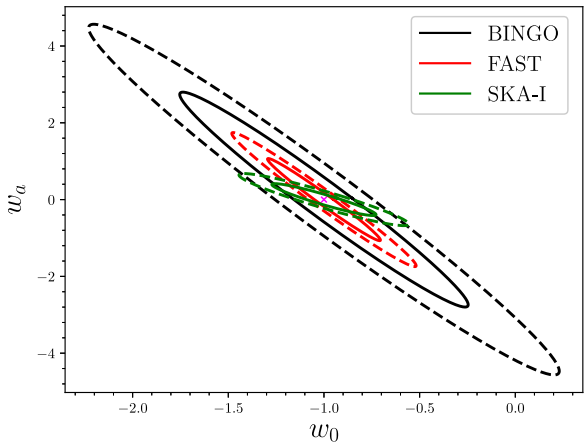

Fig. 14 Forecasts of cosmological constraints with FAST, BINGO and SKA-I with a frequency channelization of $\Delta\nu = 1$ MHz.

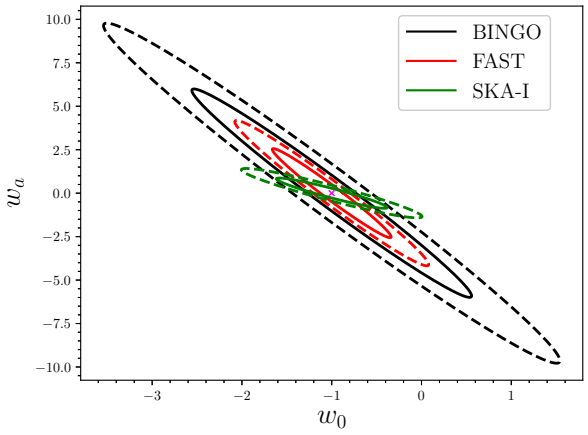

Fig. 15 w_0 versus w_a, 1σ (*solid lines*) and 2σ (*dashed lines*) cosmological constraints for FAST (*red*), BINGO (*black*) and SKA-I (*green*) for minimum multipole moment, $\ell = 10$.

ments compared to such papers as Battye et al. (2013) and Bigot-Sazy et al. (2015, 2016) to form a different forecast portfolio. Forecasting by considering various experimental designs and parameter sets is indispensable, since each set of cosmological parameters is intertwined with a particular experimental design in principle, characterizing unique prediction results with an intention to harmoniously and comparatively contribute to address caveats and pinpoint prospects as we move towards a more precise and convergent cosmology.

– Furthermore, our forecast incorporates more recent realistic and finalized development and design information because these telescope constructions have been undergoing major updates since the previous forecast results. These revisited experimental update set-ups, including the number of beams, dish diameter, frequency bandwidth coverage, survey area for FAST (see FAST included in the early study in Bull et al. (2015b)); and number of dishes for SKA-I, updated confirmed information about its precursor, MeerKAT and the new approach for modeling system temperatures.

For example, previous forecasts with SKA-I considered 190 dishes, while we make comparison, for the purpose of illustration examining the case of dark energy EoS (see Fig. 8) in terms of SKA-I performance by considering old and updated number of dishes; we use the recently accepted and confirmed dishes for SKA-I from Square Kilometre Array Cosmology Science Working Group et al. (2018) for comparative study with BINGO and FAST.

However, a number of previous forecasts were limited by the information that had been made publicly avail-

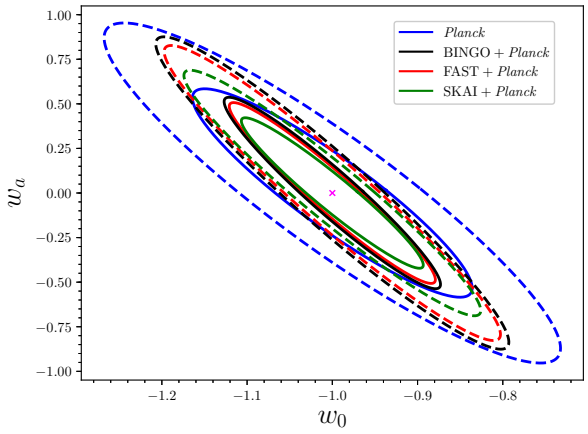

Fig. 16 w_0 versus w_a, 1σ (*solid lines*) and 2σ (*dashed lines*) cosmological constraints for *Planck* (*blue*) FAST + *Planck* (*red*), BINGO + *Planck* (*black*) and SKA-I + *Planck* (*green*) for minimum multipole moment, $\ell = 10$.

able during that time. These updates are crucial because the whole essence of the forecast is to enable the HI IM experiments to optimize their performances by considering each aspect and every single detail of their experimental designs and specifications to find out how each experiment is sensitive to various variables.

- We use a reasonably narrow and computationally effective frequency channelization, each with a bandwidth channel of $10\,\mathrm{MHz}$, in contrast to previous forecasts, such as Bull et al. (2015b) which considered $60\,\mathrm{MHz}$ for all experiments. Our consideration accounts for the role of narrower channel bandwidths, as expected for modern radio receivers (Bull et al. 2015b) in tightening the constraints.
- We forecast for an even narrower frequency channel width of $1\,\mathrm{MHz}$. This choice is close to the expected channelization of the future real HI IM surveys (Nan et al. 2011; Bigot-Sazy et al. 2016).
- To break degeneracies and improve precision of cosmological constraints, we include *Planck* 2015 CMB prior measurements that have been rigorously tested and improved. They include, CMB lensing reconstruction; TT, TE, EE *Planck* CMB (Bennett et al. 2013) power spectra, where TT represents temperature power spectrum, TE is temperature-polarization cross-spectrum, and EE is polarization power spectrum; and high ℓ CMB measurements. This aspect was not objectively considered by previous forecasts such as those that tried to include as many experiments as possible.
- We have provided more extensive quantification of cosmological constraint forecast in regard to these representative telescopes of our choice focusing on HI IM surveys. Other related works, such as Villaescusa-Navarro et al. (2017), studied the BAO measurements through single-dish HI IM observations in the post-reionization epoch in light of SKAI-MID. Shaw et al. (2014, 2015) alternatively addressed forecast of cosmological constraints, HI power spectrum estimation and measurement analyses of wide-field transient telescopes such as CHIME by an approach of what they call m-mode formalism. Furthermore, Pourtsidou et al. (2017) forecasted HI evolution with redshift and selected a subset of model-independent cosmological parameters focusing on the performance of the SKA and its precursor MeerKAT HI IM surveys (Pourtsidou 2017), proposing their cross-correlation with optical galaxy surveys. With different settings, constraints on the dark energy parameters by cross-correlating/combining SKA-like HI IM and LSST-like surveys have been calculated by Pourtsidou et al. (2015).

The essence of cross-correlating HI IM or 21 cm maps in general with galaxy redshift surveys is that contaminants, such as foregrounds, various noises and systematics between the maps from two types of surveys, are largely expected to be uncorrelated in frequency; this is in contrast to an HI signal that is correlated in respective frequency bands. Therefore, cross-correlation will not only statistically boost the abundance and the amplitude of HI signal, but will also statistically cancel out relevant foregrounds and systematics, thus increasing HI signal detection, and consequently improving constraints on the estimated values of the cosmological and astrophysical parameters. Constraints on $\Omega_{\mathrm{HI}} b_{\mathrm{HI}} r$ have a direct link on future IM survey capabilities and the prospective science outputs. These surveys heavily depend on the qualitative and quantitative measurements (such as shape and amplitude) of HI signal. Cross-correlation will thus aggregate more HI signal information than any individual experiments, yielding robust and precise cosmological measurements (Pourtsidou 2017). Pourtsidou et al. (2017), for example, have reported improvement to about a factor $\sim$ 3 by considering Stage IV spectroscopic galaxy survey (similar to *Euclid*) and MeerKAT with an overlap area of $500\,\mathrm{deg}^2$ in constraining the amplitude of the quantity $\Omega_{\mathrm{HI}} b_{\mathrm{HI}} r$, where r is a correlation coefficient that accounts for possible stochasticity in the galaxy and HI tracers (Pourtsidou 2017). Similarly, with an overlap area of $4000\,\mathrm{deg}^2$, cross-correlation between MeerKAT and Stage III photometric optical galaxy survey measured/constrained $\Omega_{\mathrm{HI}} b_{\mathrm{HI}} r$ at the $\sim$ 5 percent level across a wide range of redshifts compared to the autocorrelated MeerKAT constraints. According to them, these improvements were better than autocorrelation results they could achieve. The

fact that the cross-correlated power spectrum will be less sensitive to contaminations can be used to identify systematics in 21 cm maps (Wolz et al. 2016; Pourtsidou et al. 2017; Carucci et al. 2017). Cross-correlation could be less susceptible to systematic contaminants (Pourtsidou et al. 2015), hence foregrounds and systematics are both expected to be highly suppressed, making their removal and control much easier.

Furlanetto & Lidz (2007) have laid down several advantages of cross-correlation, and two of them are as follows: first, the SNR resulting from cross-correlating 21 cm experiments and galaxy redshift surveys exceeds that of the individual 21 cm power spectrum by a factor of a few, further asserting that this may allow probing of smaller spatial scales and possibly more efficient detection of inhomogeneous reionization, and second, the approach highly reduces the required level of foreground cleaning for the 21 cm signal/maps. The HI IM and galaxy redshift survey cross-correlation approach to suppress foregrounds and systematics has also been motivated, explored and echoed using simulations by a number of other authors, such as Wolz et al. (2016); Carucci et al. (2017); Cunnington et al. (2019). This observation is also supported by Pen et al. (2009); Chang et al. (2010); Switzer et al. (2013); Masui et al. (2013); Anderson et al. (2018) who achieved the detection of HI by cross-correlating the HI IM and optical galaxy redshift surveys. Synergized cross-correlation between these two types of surveys has mutual benefits, which make them complement each other in alleviating survey-specific systematic effects and boost HI signal detection.

Other forecasts include CMB bounds on $f_{\rm NL}$ by combining information from SKA Phase I and *Euclid*/LSST-like photometric galaxy surveys using multi-tracer approaches, contrasting with respective single-tracer measurements (Fonseca et al. 2015); and an extension of this approach for HI IM with MeerKAT and photometric galaxy survey to constrain $f_{\rm NL}$ and a number of other parameters (Fonseca et al. 2017).

– Although combination of different subsets of cosmological parameters and experimental designs largely characterize future telescope performances, this study has singled out those features that are intrinsic to the particular experiment and are likely to determine their performance reliability, consistency and stability in benchmarking with other similar surveys.

Therefore, in this paper we have intentionally addressed forecasts of cosmological constraints for the three HI IM experiments under consideration, while including issues previously not given significant attention, updating the forecasts to suit the upgrades undergone by the considered telescopes and individually and simultaneously comparatively assessing the three telescope performances while laying down a basis for any other forecast of cosmological constraints with HI IM experiments, as we prepare for real survey take-off with these next generation instruments. A great deal of such useful information that we aggregate through our research plays a complementary role in building a scientific body of knowledge that can be maximally deployed to continually study the Universe.

6 CONCLUSIONS

We have conducted forecasts for cosmological constraints (Figs. 2, 3, 9 and 11) for a set of nine cosmological parameters (Table 1) and compared performance for three different proposed future survey projects, FAST, BINGO and SKA-I. Our results, with a prescribed choice of experimental parameter set (Table 2), demonstrate that the FAST experiment will have better performance compared to BINGO, particularly in constraining dark energy EoS. Overall, SKA-I will put more stringent constraints on the dark energy EoS than FAST and BINGO. We notice that there is a trade-off between SKA-I and FAST in constraining cosmological parameters, with each experiment being more superior in constraining a particular set of parameters.

We point out that narrower frequency bandwidth such as 1 MHz (see Fig. 14) greatly improves constraints because the redshift-space-distortion effect suffers less cancelation if the frequency band becomes narrower (Hall et al. 2013; Xu et al. 2018). However, this requires more computer resources in terms of memory (RAM) for intermediate storage and speed for reasonable computational time. This challenge can be addressed by advancing computing resources and modeling strategy. We postulate that high frequency resolution needs one to take into account correlated noise residues at i-th and j-th frequency bins which would become noticeable due to many frequency channels being correlated, otherwise ignoring noise residues would be significant and in some way would impact the results. Real instrumentation will use a much narrower frequency bandwidth which would facilitate radio frequency interference excision (Nan et al. 2011).

We conclude that for a single-dish approach, BINGO, FAST and SKA-I will progressively provide stronger constraints on dark energy EoS and other cosmological parameters. The constraints can be further improved by combining with a CMB experiment such as *Planck* data.

We performed HI IM Fisher matrix forecast for BINGO, FAST and SKA-I radio telescopes, and extended similar comparative analysis for each of the three experiments' data, combined with *Planck* chains, (Planck Collaboration et al. 2014) which have considerably tight-

ened the cosmological constraints. This substantial and objective comparative analysis of simulated forecast results provides a benchmark on the relative expected performances of BINGO, FAST and SKA-I experiments under relatively similar settings in constraining an extended number of cosmological parameters in Table 1. FAST, BINGO, SKA-I and many other telescopes are suitable for HI IM, and some will even do a wider range of sciences (Nan et al. 2011) than others. Our aim is not to show the superiority or inferiority of these experiments against each other, but to illustrate a global picture on their relative prospects. Our results can, however, signal the need for adjustment, revision of specification configurations, or for further calibration where there is a possibility to rectify and optimize capabilities so that these telescopes can fulfil their promise.

This paper sets an important mark for our series of works to study IM surveys with HI. Future proceedings will feature applicability and quantification of this novel but promising approach by developing the IM pipeline to simulate sky maps for various sky emissions, addressing and testing different foreground cleaning methods, and investigating and quantifying various calibration issues. These realistic issues include bandpass calibration, systematics and other uncertainty measurements, studying and developing solid knowledge of polarization purity, and measuring BAO wiggles from HI power spectrum and consequently developing more stringent constraints on dark energy, dark matter and other cosmological parameters.

Acknowledgements E.Y. acknowledges the DAAD (German Academic Exchange Service) scholarship and financial support from The African Institute for Mathematical Sciences, University of KwaZulu-Natal, and The Dar Es Salaam University College of Education, Tanzania. Y.C.L. and Y.Z.M. acknowledge support from the National Research Foundation of South Africa (Grant Nos. 105925 and 110984).

References

Alam, S., Albareti, F. D., Allende Prieto, C., et al. 2015, ApJS, 219, 12

Alam, S., Ata, M., Bailey, S., et al. 2017, MNRAS, 470, 2617

Albrecht, A., & Bernstein, G. 2007, Phys. Rev. D, 75, 103003

Alonso, D., Bull, P., Ferreira, P. G., & Santos, M. G. 2015, MNRAS, 447, 400

Anderson, L., Aubourg, E., Bailey, S., et al. 2012, MNRAS, 427, 3435

Anderson, C. J., Luciw, N. J., Li, Y.-C., et al. 2018, MNRAS, 476, 3382

Bandura, K., Addison, G. E., Amiri, M., et al. 2014, in Society of Photo-Optical Instrumentation Engineers (SPIE) Conference Series, 9145, Proc. SPIE, 914522

Battye, R. A., Browne, I. W. A., Dickinson, C., et al. 2013, MNRAS, 434, 1239

Battye, R. A., Brown, M. L., Browne, I. W. A., et al. 2012, arXiv:1209.1041

Battye, R., Browne, I., Chen, T., et al. 2016, arXiv:1610.06826

Bennett, C. L., Larson, D., Weiland, J. L., et al. 2013, ApJS, 208, 20

Beutler, F., Blake, C., Colless, M., et al. 2011, MNRAS, 416, 3017

Bigot-Sazy, M.-A., Dickinson, C., Battye, R. A., et al. 2015, MNRAS, 454, 3240

Bigot-Sazy, M.-A., Ma, Y.-Z., Battye, R. A., et al. 2016, in Astronomical Society of the Pacific Conference Series, 502, Frontiers in Radio Astronomy and FAST Early Sciences Symposium 2015, eds. L. Qain, & D. Li, 41

Blake, C., Brough, S., Couch, W., et al. 2008, Astronomy and Geophysics, 49, 5.19

Blake, C., Kazin, E. A., Beutler, F., et al. 2011, MNRAS, 418, 1707

Braun, R., Bourke, T., Green, J. A., Keane, E., & Wagg, J. 2015, Advancing Astrophysics with the Square Kilometre Array (AASKA14), 174

Bull, P. 2016, ApJ, 817, 26

Bull, P., Camera, S., Raccanelli, A., et al. 2015a, in Advancing Astrophysics with the Square Kilometre Array (AASKA14), 24

Bull, P., Ferreira, P. G., Patel, P., & Santos, M. G. 2015b, ApJ, 803, 21

Camacho, H., Kokron, N., Andrade-Oliveira, F., et al. 2019, MNRAS, 487, 3870

Camera, S., Fonseca, J., Maartens, R., & Santos, M. G. 2018, MNRAS, 481, 1251

Carucci, I. P., Villaescusa-Navarro, F., & Viel, M. 2017, J. Cosmol. Astropart. Phys., 2017, 001

Challinor, A., & Lewis, A. 2011, Phys. Rev. D, 84, 043516

Chang, T.-C., Pen, U.-L., Bandura, K., & Peterson, J. B. 2010, Nature, 466, 463

Chang, T.-C., Pen, U.-L., Peterson, J. B., & McDonald, P. 2008, Physical Review Letters, 100, 091303

Chen, X. 2012, in International Journal of Modern Physics Conference Series, 12, 256

Chevallier, M., & Polarski, D. 2001, International Journal of Modern Physics D, 10, 213

Colless, M., Dalton, G., Maddox, S., et al. 2001, MNRAS, 328, 1039

Cunnington, S., Wolz, L., Pourtsidou, A., & Bacon, D. 2019, arXiv:1904.01479

Dark Energy Survey Collaboration, Abbott, T., Abdalla, F. B., et al. 2016, MNRAS, 460, 1270

Davis, M., Newman, J. A., Faber, S. M., & Phillips, A. C. 2001, in Deep Fields, eds. S. Cristiani, A. Renzini, & R. E. Williams, 241

DESI Collaboration, Aghamousa, A., Aguilar, J., et al. 2016, arXiv:1611.00036
Di Dio, E., Montanari, F., Durrer, R., & Lesgourgues, J. 2014, J. Cosmol. Astropart. Phys., 2014, 042
Dickinson, C. 2014, arXiv:1405.7936
Dodelson, S. 2003, Modern Cosmology (Amsterdam (Netherlands): Academic Press)
Fonseca, J., Camera, S., Santos, M. G., & Maartens, R. 2015, ApJ, 812, L22
Fonseca, J., Maartens, R., & Santos, M. G. 2017, MNRAS, 466, 2780
Furlanetto, S. R., & Lidz, A. 2007, ApJ, 660, 1030
Green, J., Schechter, P., Baltay, C., et al. 2012, arXiv:1208.4012
Hall, A., Bonvin, C., & Challinor, A. 2013, Phys. Rev. D, 87, 064026
Harper, S. E., Dickinson, C., Battye, R. A., et al. 2018, MNRAS, 478, 2416
Haynes, M. P. 2008, in Astronomical Society of the Pacific Conference Series, 395, Frontiers of Astrophysics: A Celebration of NRAO's 50th Anniversary, eds. A. H. Bridle, J. J. Condon, & G. C. Hunt, 125
Huterer, D., & Turner, M. S. 2001, Phys. Rev. D, 64, 123527
Ivezić, Ž., Kahn, S. M., Tyson, J. A., et al. 2019, ApJ, 873, 111
Jones, D. H., Read, M. A., Saunders, W., et al. 2009, MNRAS, 399, 683
Kazin, E. A., Koda, J., Blake, C., et al. 2014, MNRAS, 441, 3524
Kovetz, E. D., Viero, M. P., Lidz, A., et al. 2017, arXiv:1709.09066
Laureijs, R., Amiaux, J., Arduini, S., et al. 2011, arXiv:1110.3193
Levi, M., Bebek, C., Beers, T., et al. 2013, arXiv:1308.0847
Li, Y.-C., & Ma, Y.-Z. 2017, Phys. Rev. D, 96, 063525
Linder, E. V. 2003, Physical Review Letters, 90, 091301
Loeb, A., & Wyithe, J. S. B. 2008, Physical Review Letters, 100, 161301
LSST Science Collaboration, Abell, P. A., Allison, J., et al. 2009, arXiv:0912.0201
Masui, K. W., Switzer, E. R., Banavar, N., et al. 2013, ApJ, 763, L20
Nan, R., Li, D., Jin, C., et al. 2011, International Journal of Modern Physics D, 20, 989
Newburgh, L. B., Bandura, K., Bucher, M. A., et al. 2016, in Society of Photo-Optical Instrumentation Engineers (SPIE) Conference Series, 9906, Proc. SPIE, 99065X
Pen, U.-L., Staveley-Smith, L., Peterson, J. B., et al. 2009, MNRAS, 394, L6
Planck Collaboration, Ade, P. A. R., Aghanim, N., et al. 2014, A&A, 571, A16
Planck Collaboration, Ade, P. A. R., Aghanim, N., et al. 2016, A&A, 594, A13
Planck Collaboration, Aghanim, N., Akrami, Y., et al. 2018, arXiv:1807.06209
Pourtsidou, A. 2017, arXiv:1709.07316
Pourtsidou, A., Bacon, D., & Crittenden, R. 2015, arXiv:1506.02615
Pourtsidou, A., Bacon, D., & Crittenden, R. 2017, MNRAS, 470, 4251
Pritchard, J. R., & Loeb, A. 2012, Reports on Progress in Physics, 75, 086901
Ross, N. P., Myers, A. D., Sheldon, E. S., et al. 2012, ApJS, 199, 3
Santos, M. G., Cluver, M., Hilton, M., et al. 2017, arXiv:1709.06099
Santos, M., Bull, P., Alonso, D., et al. 2015, in Advancing Astrophysics with the Square Kilometre Array (AASKA14), 19
Shaw, J. R., & Lewis, A. 2008, Phys. Rev. D, 78, 103512
Shaw, J. R., Sigurdson, K., Pen, U.-L., Stebbins, A., & Sitwell, M. 2014, ApJ, 781, 57
Shaw, J. R., Sigurdson, K., Sitwell, M., Stebbins, A., & Pen, U.-L. 2015, Phys. Rev. D, 91, 083514
Smoot, G. F., & Debono, I. 2017, A&A, 597, A136
Square Kilometre Array Cosmology Science Working Group, Bacon, D. J., Battye, R. A., et al. 2018, arXiv:1811.02743
Switzer, E. R., Masui, K. W., Bandura, K., et al. 2013, MNRAS, 434, L46
Tansella, V., Bonvin, C., Durrer, R., Ghosh, B., & Sellentin, E. 2018, J. Cosmol. Astropart. Phys., 2018, 019
The LSST Dark Energy Science Collaboration, Mandelbaum, R., Eifler, T., et al. 2018, arXiv:1809.01669
Troxel, M. A., MacCrann, N., Zuntz, J., et al. 2018, Phys. Rev. D, 98, 043528
Villaescusa-Navarro, F., Alonso, D., & Viel, M. 2017, MNRAS, 466, 2736
Wolz, L., Abdalla, F. B., Blake, C., et al. 2014, MNRAS, 441, 3271
Wolz, L., Tonini, C., Blake, C., & Wyithe, J. S. B. 2016, MNRAS, 458, 3399
Wolz, L., Blake, C., Abdalla, F. B., et al. 2015, arXiv:1510.05453
Xu, X., Ma, Y.-Z., & Weltman, A. 2018, Phys. Rev. D, 97, 083504
York, D. G., Adelman, J., Anderson, Jr., J. E., et al. 2000, AJ, 120, 1579
Zwaan, M. A., Meyer, M. J., Webster, R. L., et al. 2004, MNRAS, 350, 1210